PAPER

Facile synthesis of a $Co_3V_2O_8$ interconnected hollow microsphere anode with superior high-rate capability for Li-ion batteries†

Yanzhu Luo,[ab] Xu Xu,[ac] Xiaocong Tian,[a] Qiulong Wei,[a] Mengyu Yan,[a] Kangning Zhao,[a] Xiaoming Xu[a] and Liqiang Mai*[a]

Hollow microspheres with a high surface area, sufficient void space, and short ion/electron transport distance have attracted much attention as a superior electrode structure for high-rate lithium-ion batteries. In this work, a facile and low-cost hydrothermal approach followed by annealing is developed to synthesize $Co_3V_2O_8$ interconnected hollow microspheres, which are able to endure an extremely high current density of 20 A g^{-1} and achieve a reversible discharge capacity of 320 mA h g^{-1}. Furthermore, a stable capacity of 424 mA h g^{-1} can be obtained after 300 cycles at 10 A g^{-1}. Such remarkable rate capability and cycling performance make the $Co_3V_2O_8$ interconnected hollow microspheres a promising anode material for lithium-ion batteries.

Introduction

Nowadays, with the rapid development of hybrid electric vehicles (HEVs) and electric vehicles (EVs), lithium-ion batteries (LIBs) with high energy and power densities, and good cyclability are in great demand.[1–4] In order to meet the requirements, various strategies have been proposed to promote the electrochemical performance, such as downsizing the particle size and[5–8] fabricating hollow micro/nanostructures.[9–11] The reduced particle size provides more electrochemically active sites and shorter transport distances for both ions and electrons, which are beneficial for the energy density and rate capability. However, the particles easily aggregate during the Li$^+$ insertion/extraction processes, leading to decreased contact with the electrolyte and rapid capacity fading.[12,13] Hollow structures can provide large electrode-electrolyte contact area and sufficient void space to alleviate the volume variation during the Li$^+$ insertion/extraction, which shows the capability to meet the challenges mentioned above.[14–17] Thus, hollow microspheres composed of primary nanoparticles would be an optimized structure for the electrode material with high energy density, high power density, and improved cycling stability.

Numerous efforts have been devoted to developing novel materials with high energy and powder densities to replace the conventional carbon based anodes.[18–32] Binary cobalt vanadates are regarded as promising candidates due to their high electrochemical activity, which results from the synergic effects of cobalt and vanadium.[24–29] Baudrin and coworkers synthesized an α-Co(VO$_3$)$_2$ anode material that can reversibly react with 9.5 lithium ions with only 17% of irreversible capacity, and a reversible capacity of 600 mA h g^{-1} can be obtained after five cycles.[25] Ultrathin $Co_3V_2O_8$ nanosheets were synthesized via a simple hydrothermal method combining with the calcination process. The resulting material is capable of delivering a specific capacity of 1114 mA h g^{-1} over 100 cycles at 1 A g^{-1}.[27] Wu and co-workers synthesized $Co_3V_2O_8 \cdot n$H$_2$O hollow hexagonal prismatic pencils through the hydrothermal method, which display a high reversible capacity of 847 mA h g^{-1} after 255 cycles at 500 mA g^{-1}.[29] Despite the progress in recent years, the high rate capability of binary cobalt vanadates still needs more improvements to meet the increasing demand for high power LIBs.

Here, we synthesized $Co_3V_2O_8$ interconnected hollow microspheres through the hydrothermal reaction combining with the calcination process. In this unique interconnected hollow microsphere architecture, the nanosized primary particles can provide short pathways for ion/electron transportation, while the hollow structure can allow sufficient penetration of the electrolyte and effectively inhibit the aggregation of primary nanoparticles. As a result, the structural integrity and conductivity of the electrode can be well maintained during the electrochemical processes. The obtained $Co_3V_2O_8$ interconnected hollow microspheres exhibit a stable discharge capacity of 424 mA h g^{-1} after 300 cycles at 10 A g^{-1}. Furthermore,

[a] State Key Laboratory of Advanced Technology for Materials Synthesis and Processing, Wuhan University of Technology, Wuhan 430070, P. R. China. E-mail: mlq518@whut.edu.cn

[b] Department of Chemical and Biomolecular Engineering, University of California, Los Angeles, California 90095, USA

[c] Department of Chemistry and Biochemistry, University of California, Los Angeles, California 90095, USA

This journal is © The Royal Society of Chemistry 2016

J. Mater. Chem. A, 2016, **4**, 5075–5080 | 5075

a reversible capability of 320 mA h g^{-1} can be obtained at a current density up to 20 A g^{-1}. Hence, we believe that the superior electrochemical performance makes the $Co_3V_2O_8$ interconnected hollow microspheres a promising anode for high power LIBs.

Experimental section

Synthesis of $Co_3V_2O_8$ interconnected hollow microspheres

To prepare $Co_3V_2O_8$ interconnected hollow microspheres, 1.495 g of cobalt acetate ($Co(CH_3COO)_2 \cdot 4H_2O$) was dispersed in 38 mL distilled water and stirred for 10 min. Subsequently, 0.468 g of ammonium vanadate (NH_4VO_3) was dissolved in deionized water with stirring at 80 °C for 15 min. After cooling down, the obtained transparent NH_4VO_3 solution was added into cobalt acetate solution slowly and stirred for another 1 h to form a reddish brown suspension. 2 mL ethylene glycol (EG) was then added. After continuous stirring for 5 h, the precursor solution was transferred into a 100 mL Teflon-lined autoclave and hydrothermally reacted at 180 °C for 24 h. The resulting products were collected by centrifugation, washed with deionized water and ethanol, and dried at 80 °C in air. Finally, the obtained precursor was sintered at 450 °C for 10 h in air to get brown $Co_3V_2O_8$ interconnected hollow microspheres, which are denoted as $Co_3V_2O_8$-IHMs. The control sample was prepared under the same synthetic conditions except for the addition of EG, which is labelled as $Co_3V_2O_8$-SMPs (solid microparticles) in the following description.

Characterization

X-ray powder diffraction (XRD) was conducted on a Bruker D8 Discover with a non-monochromated Co Kα X-ray source. Field emission scanning electron microscopy (FESEM, JEOL JSM-7100F) and high-resolution transmission electron microscopy (HRTEM, JEOL JEM-2100F) were applied to characterize the morphologies of the samples. X-ray photoelectron spectroscopy analysis was conducted on a VG Multilab 2000 system. The Brunauer–Emmett–Teller (BET) specific surface area and Barrett–Joyner–Halenda (BJH) pore size distribution were analyzed using a Micromeritics Tristar 3020 instrument at 77 K.

Electrochemical measurements

A CR2025-type coin cell with a lithium foil as the anode was assembled to evaluate the electrochemical performance on a LAND battery testing system (CT2001A). To prepare the working electrode, 70 wt% active material ($Co_3V_2O_8$-IHMs and $Co_3V_2O_8$-SMPs), 20 wt% acetylene black (Super-P), and 10 wt% sodium alginate were mixed in deionized water to form a slurry. Then the slurry was coated onto a copper foil using a blade with the same height every time to make sure that the thickness of the slurry was constant. The electrode was dried at 120 °C overnight under air. The obtained electrode was punched into circular disks with an average mass loading of the active material of 2 mg cm^{-2}. The electrolyte is composed of 1 M $LiPF_6$ in ethylene carbon (EC)/dimethyl carbonate (DMC) with a volume ratio of 1 : 1. Cyclic voltammetry (CV) tests were carried out on a CHI 760D electrochemical workstation. All of the electrochemical tests were performed in the voltage range from 0.01 to 2.50 V. Electrochemical impedance spectroscopy (EIS) was carried out using an Autolab PGSTAT 302N electrochemical workstation (cell voltage of 2.20 V, frequency range from 100 kHz to 0.01 Hz). All of the tests were performed at room temperature.

Results and discussion

The overall schematic illustration of the fabrication process of $Co_3V_2O_8$-IHMs and $Co_3V_2O_8$-SMPs is depicted in Fig. 1. The aqueous solution containing $Co(CH_3COO)_2 \cdot 4H_2O$ and NH_4VO_3 are mixed in step A, while step B is the determinative step for the two different synthetic processes, as $Co_3V_2O_8$-SMPs are synthesized without EG. In order to explore the growth mechanism, time-dependent experiments were carried out to track the phase and morphology transformation during the synthetic process. During step A, the reddish brown precipitate emerges quickly after the addition of NH_4VO_3, which is confirmed as aggregated particles composed of 200–300 nm secondary particles with smooth surface (Fig. S1A†). According to SEM images, the particle size remains steady in the following stirring procedure (Fig. S1B and C†). Afterwards, the $Co_3V_2O_8$-IHM precursor solution is continuously stirred for another 4 hours (step B) after the addition of EG and the particle size of the resultant particles slightly increases, while the morphology of $Co_3V_2O_8$-SMP precursor particles remains unchanged (Fig. S2A–H†). After the hydrothermal treatment, the $Co_3V_2O_8$-IHM precursor particles transform into hierarchical microspheres comprised of primary particles, and the microsphere's size generally increases to about two times larger than that of the original one (Fig. S2G and H†), while the round shaped $Co_3V_2O_8$-SMP precursor particles turn into cubic nanoparticles with an almost unchanged particle size after the hydrothermal reaction (Fig. S2I†). After calcination, the morphology of $Co_3V_2O_8$-IHM precursor particles is well preserved, which turns out to be interconnected hollow microspheres (Fig. S3A†). However, the $Co_3V_2O_8$-SMP cubic precursor particles change dramatically and transform into irregular solid microparticles due to the high surface energy of the cubic precursor nanoparticles (Fig. S3B and C†).

Obviously, EG is the key factor for the formation of interconnected hollow microspheres. During step A, the initial small primary nanoparticles aggregate to minimize the total energy of the system. EG molecules are determined as ligands with abundant hydroxy groups to coordinate with metal ions into metal glycolate.[33] As a result, after the addition of EG, it would form a layer on the surface of primary nanoparticles. During the hydrothermal reaction in step C, the small crystallites in the core region gradually dissolve and successively recrystallize in the outermost surface under the relatively high temperature and vapor pressure, which is well known as the inside-out Ostwald ripening process.[34–36] During the recrystallization process, EG would induce the assembly and growth process of the recrystallized particles. Furthermore, the chelates of EG would control the particle growth and prevent particle agglomeration. However,
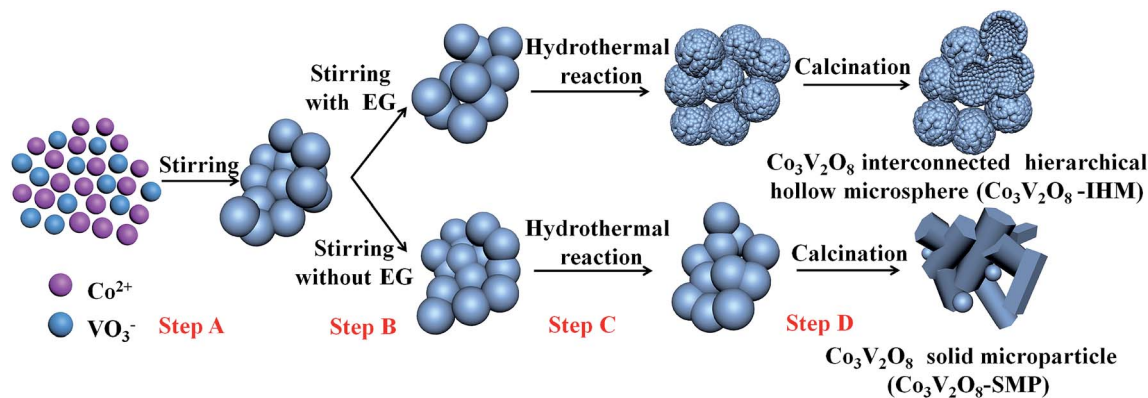
5076 | J. Mater. Chem. A, 2016, **4**, 5075–5080

This journal is © The Royal Society of Chemistry 2016

Fig. 1 Schematic illustration of the synthesis of $Co_3V_2O_8$-IHMs and $Co_3V_2O_8$-SMPs.

driven by the minimization of interfacial energy, the resulting recrystallized particles would form a low-energy configuration interface and become compact.[35] As a result, the $Co_3V_2O_8$-IHM comprising small primary particles with an increased spherical radius and interconnected hollow structure is obtained. The XRD patterns of the as-prepared precursor particles are shown in Fig. S4.† It is interesting that $Co_3V_2O_8$-IHM precursor particles show strong characteristic peaks of orthorhombic $Co_3V_2O_8$ (JCPDS card No. 01-016-0832), which are the same as those of the sample after the calcination (Fig. 2A). However, $Co_3V_2O_8$-SMP precursor particles present an amorphous structure without any obvious peaks. The results show that EG also plays an important role in the subsequent oligomerization of the composite during the hydrothermal process.[33]

Both $Co_3V_2O_8$ samples were first investigated by XRD, and the patterns are shown in Fig. 2A. For both samples, all of the diffraction peaks can be indexed to orthorhombic $Co_3V_2O_8$ (JCPDS card No. 01-016-0832). XPS spectra shown in Fig. S5† further verify the coexistence of Co^{2+}, V^{5+}, and O^{2-} in $Co_3V_2O_8$.[29] Compared with $Co_3V_2O_8$-SMPs, $Co_3V_2O_8$-IHMs exhibit a broader half-width and lower peak intensity, indicating the nanosized primary particles of $Co_3V_2O_8$-IHMs, which is consistent with the corresponding SEM and TEM images (Fig. 2B and E).[37,38] The corresponding elemental mapping images of $Co_3V_2O_8$-IHMs indicate the highly uniform distribution of cobalt, vanadium, and oxygen in the final product (Fig. 2C). The interconnected hierarchical hollow feature can be easily recognized as the large void space in the interior of the microsphere which shows relatively low contrast in the TEM image (Fig. 2D and E). The typical HRTEM image of $Co_3V_2O_8$-IHMs is shown in Fig. 2F. The primary nanoparticles are tightly attached to each other during the formation of the interconnected hollow microspheres. Moreover, the atomic spacing of 0.25 and 0.30 nm can be clearly discerned, corresponding to the (122) and (131) lattice fringes of orthorhombic $Co_3V_2O_8$, respectively. As determined by nitrogen adsorption–desorption measurements (Fig. S6†), the $Co_3V_2O_8$-IHMs show a specific surface area of 26 m^2 g^{-1} with a pore volume of 0.11 cm^3 g^{-1}, which is much higher than that of $Co_3V_2O_8$-SMPs (low surface area of 1.4 m^2 g^{-1} with a pore volume of 0.0082 cm^3 g^{-1}).
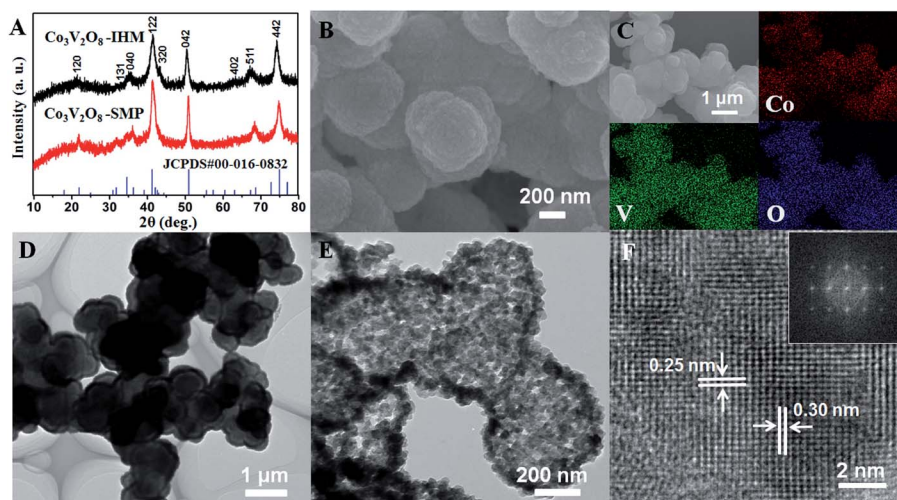
Fig. 2 (A) XRD patterns of $Co_3V_2O_8$-IHMs and $Co_3V_2O_8$-SMPs. SEM images (B) and the corresponding elemental mapping images of cobalt, vanadium, and oxygen in the $Co_3V_2O_8$-IHMs (C), (D–F) TEM and HRTEM images, and FFT pattern of $Co_3V_2O_8$-IHMs.
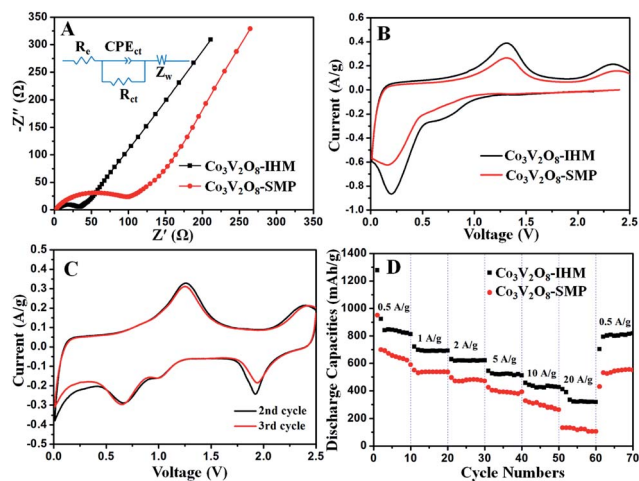
Fig. 3 (A) The typical Nyquist plots of $Co_3V_2O_8$-IHMs and $Co_3V_2O_8$-SMPs before cycling. The inset shows the equivalent circuit. (B) First cycle of cyclic voltammetry curves of $Co_3V_2O_8$-IHMs and $Co_3V_2O_8$-SMPs at a sweep rate of 0.1 mV s^{-1} in the potential range from 0.01 to 2.5 V vs. Li/Li$^+$. (C) Second and third cycles of cyclic voltammetry curves of $Co_3V_2O_8$-IHMs at a sweep rate of 0.1 mV s^{-1} in the potential range from 0.01 to 2.5 V vs. Li/Li$^+$. (D) The rate performance of the $Co_3V_2O_8$-IHMs and $Co_3V_2O_8$-SMPs at different current densities.
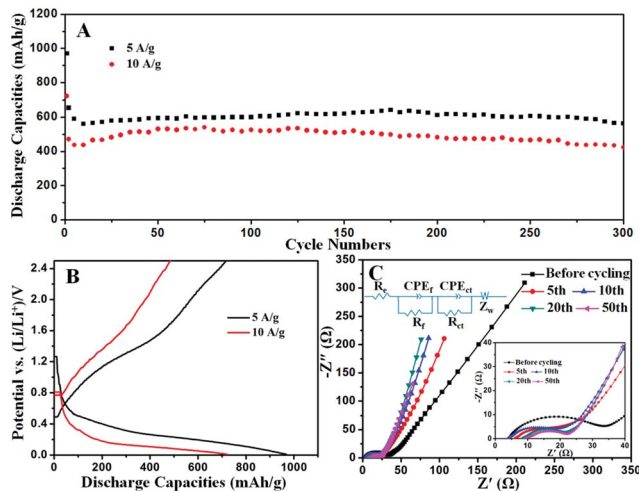
Fig. 4 (A) Cycling performance of $Co_3V_2O_8$-IHMs at current densities of 5 A g^{-1} and 10 A g^{-1} for 300 cycles. (B) The first cycle charge/discharge profiles at current densities of 5 A g^{-1} and 10 A g^{-1}. (C) The typical Nyquist plots of $Co_3V_2O_8$-IHMs before cycling and after different cycles.

Accordingly, the BJH pore size distribution plot displays a maximum peak at ca. 20 nm, which is mainly from the interparticle voids in the shell (Fig. S6†).

It is reported that the interconnected hollow microsphere structure would facilitate the transportation of the electrons and ions.[9,13] The detailed reaction kinetics of both samples are compared using electrochemical impedance spectroscopy (EIS) (Fig. 3A). The equivalent circuit is displayed in the inset of Fig. 3A, where R_e is the equivalent series resistance, R_{ct} is the charge transfer resistance, and CPE_{ct} is the capacitance related to the

double layer, while Z_w corresponds to the Warburg impedance associated with the diffusion of the lithium ions.[39] The result shows that the charge transfer resistance (R_{ct}) values of $Co_3V_2O_8$-IHM and $Co_3V_2O_8$-SMP samples before cycling are 30 and 99 Ω, respectively. The lower resistance of $Co_3V_2O_8$-IHMs is beneficial for the battery performance, especially the high-rate capability, which is further verified in the following discussion.

Furthermore, CV curves of $Co_3V_2O_8$-IHMs and $Co_3V_2O_8$-SMPs are investigated at a scan rate of 0.1 mV s^{-1} in the potential window of 0.01–2.5 V (Fig. 3B and C). It is clear that both samples exhibit similar CV curves, while $Co_3V_2O_8$-IHMs exhibit less polarization, a larger curve area, and higher redox currents than $Co_3V_2O_8$-SMPs. The results suggest that $Co_3V_2O_8$-IHMs present better utilization of the active material and lower barrier for charge transfer and Li-ion diffusion.[37,40] The peak around 0.77 V in the discharge process might be associated with the decomposition of $Co_3V_2O_8$ ($Co_3V_2O_8 \rightarrow 3CoO + V_2O_5$), and the lithiation of V_2O_5 ($V_2O_5 + xLi^+ + xe^- \rightarrow Li_xV_2O_5$). Upon deeper lithiation, the reactions at around 0.2 V correspond to the formation of metallic Co from CoO nanoparticles ($CoO + 2Li^+ + 2e^- \rightarrow Co + Li_2O$), further lithiation of $Li_xV_2O_5$ ($Li_xV_2O_5 + yLi^+ + ye^- \rightarrow Li_{x+y}V_2O_5$), and the formation of a solid electrolyte interface (SEI). The peaks at 1.3 V and 2.34 V in the charge process correspond to the reversible insertion of extracted lithium ions into $Li_xV_2O_5$ and formation of CoO from metallic Co.[27] During the charge/discharge process, it is clear that the initial CV curve is quite different from those of the subsequent cycles (Fig. 3B and C). This phenomenon is due to the irreversible decomposition of the electrolyte and the $Co_3V_2O_8$ crystal structure during the first cycle.[41] In the lithium intercalation/extraction process of the following cycles, three cathodic peaks at 1.92, 1.02, and 0.65 V and two anodic peaks at 1.26 and 2.40 V are observed, respectively (Fig. 3C). During the third cycle, there is a slight shift of cathodic peaks to higher potentials, indicating an easier reduction process, which might be attributed to the activation effect in the first two cycles.[42,43] The identical electrochemical reaction in the following cycles demonstrates the reversible transformation between Co and CoO, combining with the lithiation/delithiation of vanadium oxide.

The rate capability of $Co_3V_2O_8$-IHMs and $Co_3V_2O_8$-SMPs was investigated with the current densities gradually increasing from 0.5 to 20 A g^{-1} and then reducing back to 0.5 A g^{-1} (Fig. 3D). $Co_3V_2O_8$-IHMs exhibit a remarkable rate performance at various current densities. The second cycle discharge capacities are 923, 698, 618, 526, 443, and 390 mA h g^{-1} at 0.5, 1, 2, 5, 10 and 20 A g^{-1}, respectively. Furthermore, the reversible capacity can be stabilized at about 320 mA h g^{-1} at 20 A g^{-1} during the rate performance test. It is noteworthy that when the current density reduces to 0.5 A g^{-1}, a reversible average capacity of 794 mA h g^{-1} can be recovered for the $Co_3V_2O_8$-IHMs. The corresponding charge/discharge profiles of $Co_3V_2O_8$-IHMs and $Co_3V_2O_8$-SMPs at different current densities are shown in Fig. S7A and B,† respectively. The better rate capability of $Co_3V_2O_8$-IHMs further confirms the advantage of our rationally designed interconnected hollow microsphere structure.

The high-rate and long-life cycling performance of $Co_3V_2O_8$-IHMs is further investigated (Fig. 4A). The reversible discharge
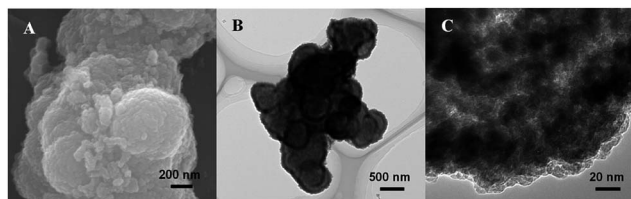
Fig. 5 *Ex situ* SEM (A) and TEM (B and C) images collected at a voltage of 0.01 V after 10 cycles.

capacities of 654 and 470 mA h g^{-1} can be achieved at a rate of 5 and 10 A g^{-1}, respectively. It is interesting that the capacities increase gradually after the initial decrease, which has been observed in the reported studies.[44–46] The CV results suggest that the original Co$_3$V$_2$O$_8$ structure transforms into nanocrystalline CoO combining with the formation of the SEI during the electrochemical process, leading to a lower conductivity of active materials as well as the initial capacity decrease. However, along with further cycling, the unused active material would be fully utilized, resulting in increased capacity. The corresponding first cycle voltage capacity profiles at current densities of 5 A g^{-1} and 10 A g^{-1} are shown in Fig. 4B. It is worth noting that a high discharge capacity of 424 mA h g^{-1} can be obtained at a high current density of 10 A g^{-1} after 300 cycles, corresponding to the capacity retention of 90% from the 2nd to the 300th cycle (an average loss of only 0.035% per cycle). The excellent high Li$^+$ storage capability and good cyclability of the anode material can be attributed to the full usage of the active material (sufficient contact area with the electrolyte caused by voids between primary particles on the shell) and the stable structure (hollow structure provides sufficient space for the volume expansion/extraction during the electrochemical process).

In order to further understand the origin of the superior electrochemical performance of Co$_3$V$_2$O$_8$-IHMs, the detailed reaction kinetics of the Co$_3$V$_2$O$_8$-IHMs at a voltage of 2.2 V before cycling and at the 5th, 10th, 20th, and 50th cycles were investigated by EIS (Fig. 4C). Quantitative analysis after cycles was carried out by fitting the AC impedance spectra using an equivalent circuit (inset of Fig. 4C), which is different from that of Fig. 3A. This can be attributed to the increased depressed semicircles at high frequencies along with the increased cycles, which is caused by the formation of a SEI layer on the surface of active materials.[39] The calculated R_f and R_{ct} values are displayed in Table S1,† which clearly show that the SEI increases gradually with the cycling process and becomes stable after 20 cycles as the EIS plot after 20 and 50 cycles presents a very similar feature. It is noteworthy that the R_{ct} of the fifth cycle decreases drastically compared with that of the fresh electrode, as the electrochemical reaction improves the penetration of the electrolyte into the electrode, leading to reduced interfacial impedance between the electrode and electrolyte.[20] However, the charge transfer resistance is stabilized after the fifth cycle, indicating that the unique interconnected hollow microsphere structure could facilitate the activation process and preserve the original morphology with abundant voids for the electron/ion transportation. In order to verify the speculation, *ex situ* SEM and TEM were conducted to investigate the morphological and structural changes after ten cycles at the fully discharged state (Fig. 5). The hierarchical hollow microsphere structure is well retained after the electrochemical reaction, indicating a high mechanical flexibility to accommodate the volume expansion during cycling. On the basis of the results above, the superior high-rate and cycling performance of Co$_3$V$_2$O$_8$-IHMs can be attributed to the unique hierarchical hollow microsphere structure with high mechanical flexibility and efficient electron/ion transportation pathway.

Conclusions

In summary, Co$_3$V$_2$O$_8$ interconnected hollow microspheres have been successfully synthesized using a facile hydrothermal reaction followed by annealing in air atmosphere. EG plays a key role in the formation of the hollow structure with interconnected open pores in the shell, providing a fast and short electron/ion transportation pathway, sufficient electrolyte penetration, and high mechanical flexibility. This novel Co$_3$V$_2$O$_8$ interconnected hollow microsphere anode exhibits excellent rate capability (320 mA h g^{-1} at 20 A g^{-1}), and good cycling stability (424 mA h g^{-1} can still be obtained after 300 cycles at 10 A g^{-1}). These results suggest that the interconnected hollow microsphere anode represents a promising candidate for practical applications, and this facile method can be extended to synthesize other binary metal oxide interconnected hollow microspheres with excellent electrochemical performance.

Acknowledgements

Notes and references

1 X. D. Xu, R. G. Cao, S. Jeong and J. Cho, *Nano Lett.*, 2012, **12**, 4988–4991.
2 Y. M. Sun, X. L. Hu, W. Luo, F. F. Xia and Y. H. Huang, *Adv. Funct. Mater.*, 2013, **23**, 2436–2444.
3 F. F. Cao, J. W. Deng, S. Xin, H. X. Ji, O. G. Schmidt, L. J. Wan and Y. G. Guo, *Adv. Mater.*, 2011, **23**, 4415–4420.
4 J. Liu, K. P. Song, P. A. van Aken, J. Maier and Y. Yu, *Nano Lett.*, 2014, **14**, 2597–2603.
5 L. F. Shen, X. G. Zhang, E. Uchaker, C. Z. Yuan and G. Z. Cao, *Adv. Energy Mater.*, 2012, **2**, 691–698.
6 J. S. Chen and X. W. Lou, *Small*, 2013, **9**, 1877–1893.
7 Y. Y. Li, H. Y. Zhang and P. K. Shen, *Nano Energy*, 2015, **13**, 563–572.

8 V. Raju, J. Rains, C. Gates, W. Luo, X. F. Wang, W. F. Stickle, G. D. Stucky and X. L. Ji, *Nano Lett.*, 2014, **14**, 4119–4124.

9 J. Jin, S. Z. Huang, J. Shu, H. E. Wang, Y. Li, Y. Yu, L. H. Chen, B. J. Wang and B. L. Su, *Nano Energy*, 2015, **16**, 339–349.

10 Y. Xia, Z. Xiao, X. Dou, H. Huang, X. H. Lu, R. J. Yan, Y. P. Gan, W. J. Zhu, J. P. Tu, W. K. Zhang and X. Y. Tao, *ACS Nano*, 2013, **7**, 7083–7092.

11 S. M. Xu, C. M. Hessel, H. Ren, R. B. Yu, Q. Jin, M. Yang, H. J. Zhao and D. Wang, *Energy Environ. Sci.*, 2014, **7**, 632–637.

12 Z. S. Wu, W. C. Ren, L. Wen, L. B. Gao, J. P. Zhao, Z. P. Chen, G. M. Zhou, F. Li and H. M. Cheng, *ACS Nano*, 2010, **4**, 3187–3194.

13 D. L. Wang, Y. C. Yu, H. He, J. Wang, W. D. Zhou and H. D. Abruna, *ACS Nano*, 2015, **9**, 1775–1781.

14 J. Y. Wang, N. L. Yang, H. J. Tang, Z. H. Dong, Q. Jin, M. Yang, D. Kisailus, H. J. Zhao, Z. Y. Tang and D. Wang, *Angew. Chem., Int. Ed.*, 2013, **52**, 6417–6420.

15 L. Zhou, H. B. Wu, T. Zhu and X. W. Lou, *J. Mater. Chem.*, 2012, **22**, 827–829.

16 L. Zhang, J. F. Ni, W. C. Wang, J. Guo and L. Li, *J. Mater. Chem. A*, 2015, **3**, 11782–11786.

17 Y. Yao, M. T. McDowell, I. Ryu, H. Wu, N. Liu, L. Hu, W. D. Nix and Y. Cui, *Nano Lett.*, 2011, **11**, 2949–2954.

18 Q. D. Li, Q. L. Wei, J. Z. Sheng, M. Y. Yan, L. Zhou, W. Luo, R. M. Sun and L. Q. Mai, *Adv. Sci.*, 2015, **2**, 1500284.

19 H. T. Sun, G. Q. Xin, T. Hu, M. P. Yu, D. L. Shao, X. Sun and J. Lian, *Nat. Commun.*, 2014, **5**, 4526.

20 M. L. Li, X. Yang, C. Z. Wang, N. Chen, F. Hu, X. F. Bie, Y. J. Wei, F. Du and G. Chen, *J. Mater. Chem. A*, 2015, **3**, 586–592.

21 C. J. Niu, J. S. Meng, C. H. Han, K. N. Zhao, M. Y. Yan and L. Q. Mai, *Nano Lett.*, 2014, **14**, 2873–2878.

22 Y. Z. Jiang, D. Zhang, Y. Li, T. Z. Yuan, N. Bahlawane, C. Liang, W. P. Sun, Y. H. Lu and M. Yan, *Nano Energy*, 2014, **4**, 23–30.

23 L. Q. Mai, X. Xu, L. Xu, C. H. Han and Y. Z. Luo, *J. Mater. Res.*, 2011, **26**, 2175–2185.

24 S. Denis, E. Baudrin, F. Orsini, G. Ouvrard, M. Touboul and J. M. Tarascon, *J. Power Sources*, 1999, **81**, 79–84.

25 E. Baudrin, S. Laruelle, S. Denis, M. Touboul and J. M. Tarascon, *Solid State Ionics*, 1999, **123**, 139–153.

26 Y. Tang, J. Zhou, J. Liu, L. X. Liu and S. Q. Liang, *Int. J. Electrochem. Sci.*, 2013, **8**, 1138–1145.

27 G. Z. Yang, H. Cui, G. W. Yang and C. X. Wang, *ACS Nano*, 2014, **8**, 4474–4487.

28 F. F. Wu, C. H. Yu, W. X. Liu, T. Wang, J. K. Feng and S. L. Xiong, *J. Mater. Chem. A*, 2015, **3**, 16728–16736.

29 F. F. Wu, S. L. Xiong, Y. T. Qian and S. H. Yu, *Angew. Chem., Int. Ed.*, 2015, **54**, 10787–10791.

30 H. Wu, M. Xu, Y. C. Wang and G. F. Zheng, *Nano Res.*, 2013, **6**, 167–173.

31 H. Jiang, H. X. Zhang, Y. Fu, S. J. Guo, Y. J. Hu, L. Zhang, Y. Liu, H. L. Liu and C. Z. Li, *ACS Nano*, 2016, **10**, 1648–1654.

32 H. Jiang, D. Y. Ren, H. F. Wang, Y. J. Hu, S. J. Guo, H. Y. Yuan, P. J. Hu, L. Zhang and C. Z. Li, *Adv. Mater.*, 2015, **27**, 3687–3695.

33 A. M. Cao, J. S. Hu, H. P. Liang and L. J. Wan, *Angew. Chem., Int. Ed.*, 2005, **44**, 4391–4395.

34 B. Wang, H. B. Wu, L. Zhang and X. W. Lou, *Angew. Chem., Int. Ed.*, 2013, **52**, 4165–4168.

35 R. Qiao, X. L. Zhang, R. Qiu, J. C. Kim and Y. S. Kang, *Chem.–Eur. J.*, 2009, **15**, 1886–1892.

36 Y. C. Chen, L. Hu, M. Wang, Y. L. Min and Y. G. Zhang, *Colloids Surf., A*, 2009, **336**, 64–68.

37 D. P. Lv, M. L. Gordin, R. Yi, T. Xu, J. X. Song, Y. B. Jiang, D. Choi and D. H. Wang, *Adv. Funct. Mater.*, 2014, **24**, 1059–1066.

38 X. F. Gao, Y. J. Sha, Q. Lin, R. Cai, M. O. Tade and Z. P. Shao, *J. Power Sources*, 2015, **275**, 38–44.

39 H. X. Ji, L. L. Zhang, M. T. Pettes, H. F. Li, S. S. Chen, L. Shi, R. Piner and R. S. Ruoff, *Nano Lett.*, 2012, **12**, 2446–2451.

40 X. Xu, Y. Z. Luo, L. Q. Mai, Y. L. Zhao, Q. Y. An, L. Xu, F. Hu, L. Zhang and Q. J. Zhang, *NPG Asia Mater.*, 2012, **4**, e20.

41 L. Yu, L. Zhang, H. B. Wu, G. Q. Zhang and X. W. Lou, *Energy Environ. Sci.*, 2013, **6**, 2664–2671.

42 Z. Y. Wang, L. Zhou and X. W. Lou, *Adv. Mater.*, 2012, **24**, 1903–1911.

43 G. N. Zhu, Y. G. Wang and Y. Y. Xia, *Energy Environ. Sci.*, 2012, **5**, 6652–6657.

44 G. X. Gao, L. Yu, H. B. Wu and X. W. Lou, *Small*, 2014, **10**, 1741–1745.

45 Q. Y. An, F. Lv, Q. Q. Liu, C. H. Han, K. N. Zhao, J. Z. Sheng, Q. L. Wei, M. Y. Yan and L. Q. Mai, *Nano Lett.*, 2014, **14**, 6250–6256.

46 N. Zhang, Q. Zhao, X. P. Han, J. G. Yang and J. Chen, *Nanoscale*, 2014, **6**, 2827–2832.

5080 | *J. Mater. Chem. A*, 2016, **4**, 5075–5080

This journal is © The Royal Society of Chemistry 2016